Modeling of freak wave generation in a 3D-NWT *

Carlo Brandini [1], *and Stéphan Grilli* [2]

1. Dipartimento di Ingegneria Civile, Università degli Studi di Firenze, Via di Santa Marta 3, 50139 Firenze, ITALY

2. Department of Ocean Engineering, University of Rhode Island, Narragansett, RI 02882, USA

ABSTRACT

Freak waves are extreme ocean waves that are not predicted by traditional wave probability distributions. We study wave energy focusing, as a possible mechanism for freak wave formation, in a three-dimensional (3D) Numerical Wave Tank (NWT) solving fully nonlinear potential flow equations. The NWT combines a higher-order 3D-BEM and a Mixed-Eulerian-Lagrangian time updating of the free surface, based on explicit second-order Taylor series expansions. Self-focusing of wave energy is achieved through modulating a periodic wave train in two orthogonal directions. This process is first carried out using a Higher Order Spectral method whose solution is then introduced in the NWT, in which we specify space periodicity conditions on lateral boundaries. Directional and frequency focusing of wave energy are achieved through using a snake wavemaker to generate curved wave fronts at one extremity of the NWT, and specifying an actively absorbing open boundary condition at the other extremity of the NWT. Breaking and non-breaking freak waves are generated in the NWT and their shape and kinematics are studied.

KEYWORDS : freak waves, numerical wave tank, nonlinear wave transformations, wave energy focusing, boundary element method.

INTRODUCTION

In recent years, due to the building of increasingly large ocean structures in increasingly deeper waters, it has become very important to predict both the shape and kinematics, and the conditions of occurrence of the largest ocean waves, which may be very damaging, despite their low probability of occurrence. These waves, often referred to as "freak waves", are far steeper than predicted by the Rayleigh distribution (e.g., Sand *et al.*, 1990; Skourup,*et al.*, 1997), and are highly transient waves, believed to result from the focusing of wave energy, whereby phases and directions of individual wave components are such that constructive interference occurs in a small region of space and time (e.g., Baldock and Swan, 1994). Whereas wave energy focusing can occur as a result of the bottom topography (i.e., over a shallow shoal) or due to wave-current interactions leading to the formation of a caustic region (White and Fornberg, 1998), we will concentrate on cases with no current, and of deep or constant water depth, thus eliminating bottom effects. These cases include those where wave energy focusing occurs due to self-focusing instabilities, or to directional effects with or without frequency dispersion effects, both in the presence of nonlinear wave-wave interactions, producing waves larger than obtained by linear superposition (Dean, 1990).

Freak waves have been observed to be essentially three-dimensional (3D) phenomena. Nepf *et al.* (1998), for instance, experimentally showed that curved wave fronts lead to 3D breaking in ocean waves, and that the shape and kinematics of 3D breaking waves greatly differ from those of two-dimensional (2D) breakers (see also She *et al.*, 1997; and Johannessen and Swan, 1998). McLean (1982) theoretically predicted a type of wave instability (called type II), which is predominantly 3D, in contrast with the 2D instability (type I; i.e., the side-band instability) identified by Benjamin and Feir (1967), which leads to the formation of wave groups in quasi-2D swells, through a self-focusing mechanism. Su *et al.* (1982) experimentally confirmed this prediction by showing how a steep 2D wave train can evolve into 3D spilling breakers. Hence, 3D modulational instabilities cannot be neglected when describing the steepest ocean waves. Two-dimensional nonlinear wave instabilities have been simulated in a few numerical studies, by slow self-modulations of a 2D periodic wave train (e.g., Dold and Peregrine, 1986; Dysthe *et al.*, 1999; Henderson *et al.*, 1999). In such studies, an ini-

*To appear in *Proc. ISOPE 2001 Conf.* (Stavanger, Norway)

tially periodic wave train of moderate steepness is perturbed by a small periodic perturbation. After a large time of propagation (typically over 100 wave periods), it is observed that a large steep wave, i.e., a freak wave, may emerge from the initial wave train, and break or recede and periodically reappear. In these studies, 3D effects were not usually addressed because, either it was not possible to generalize the method of solution to 3D, or the computational effort in a 3D model was too high.

Alternately, instead of analizing slow perturbations of wave trains as they occur in nature, which may not be very easy or even impossible to achieve (for instance in the laboratory), large transient (sometimes breaking) waves have been produced in 2D laboratory wave tanks, and in 2D fully nonlinear numerical wave models, by simulating frequency focusing using wavemakers (e.g., Chaplin, 1996; Dommermuth *et al.*, 1988; Kjeldsen *et al.*, 2000). In this process, shorter waves are first generated, followed by longer waves which, due to frequency dispersion, are faster and catch up with the shorter waves over some small area of space, thus producing a very large wave through superposition. As pointed out by Dean (1990), nonlinear wave-wave interations both further reinforce energy focusing, leading to formation an even larger wave, and add amplitude dispersion to the wave components, thus also making frequency focusing at a single point harder to achieve. In 3D wave tanks, energy focusing has been achieved by making a large number of directional wave components, usually of the same frequency, converge into a small region of the tank. In practice, a snake wavemaker motion is prescribed according to linear wave theory (Dalrymple, 1989), such as to generate curved wave fronts and focus wave energy at a specified distance away from the wavemaker. She *et al.* (1997) used such a method in laboratory experiments, to produce 3D directional wave focusing and study extreme wave kinematics. As said before, nonlinear wave-wave interactions will also reinforce directional wave focusing. Brandini and Grilli (2000), for instance, presented first- and second-order analytic solutions of the directional wave focusing problem, by superposing periodic 3D Stokes waves of the corresponding order. Fig. 1, for instance, shows such a second-order solution. Comparing this solution with that obtained by linear superposition, we would see that the height and steepness of the large wave produced in the middle of the domain are significantly increased.

In light of this brief review of the state-of-the-art in freak wave modeling and analysis, the purpose of the present work is two-fold : (i) developing a fully nonlinear 3D model simulating physical mechanisms leading to freak wave generation over constant depth, through energy focusing (including self- and frequency/directional focusing); and (ii), based on results obtained in (i), producing extreme, possibly breaking, waves and studying their kinematics. This will be achieved by modifying and using an accurate 3D fully nonlinear potential flow model (i.e., a "Numerical Wave Tank"; NWT), recently developed by Grilli *et al.* (2000,2001). This model combines a higher-order Boundary Element Method (BEM),

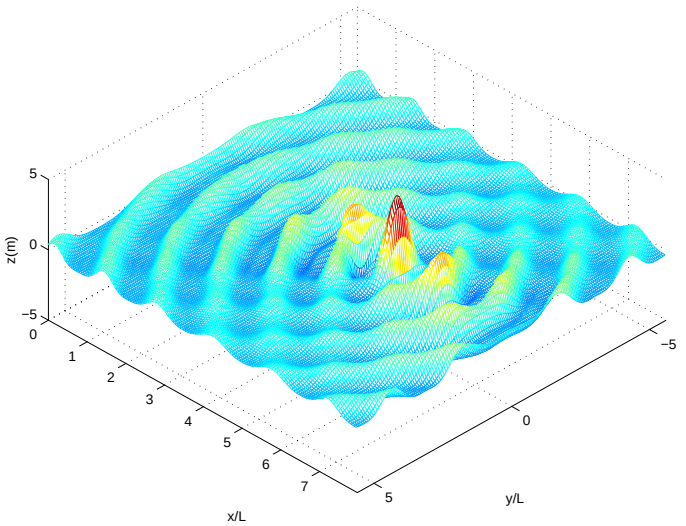

Fig. 1 : Example of second-order directional wave focusing through Stokes wave superposition (Brandini and Grilli, 2000).

with an Eulerian-Lagrangian flow representation, and an explicit time updating. Wave overturning can be simulated in this NWT, up to impact of a breaker jet on the free surface. In the present case, due to constant water depth, for more efficiency of the computations, the image method is used to eliminate the bottom boundary discretization. A snake wavemaker motion is modeled at one extremity of the NWT, in order to generate directional wave trains. A new actively absorbing open boundary condition is modeled at the far end of the NWT, which is an extension of Clément's (1996) 2D "absorbing piston" condition, to a 3D "snake absorbing piston" boundary.

Grilli *et al.* validated their 3D-NWT for solitary wave shoaling and breaking over slopes, by comparing results to experiments and to an earlier numerical solution. The agreement was excellent and it was found that almost arbitrary accuracy could be obtained in the computations by carefully selecting the discretization of the simulation domain.

We model wave energy focusing two ways in the 3D-NWT.

- First, we study wave trains subjected to both longitudinal and lateral modulations over long times of propagation, leading to self-focusing of wave energy. To limit the computational cost in the 3D-NWT, the computationally efficient "Higher Order Spectral" (HOS) method, developed by Dommermuth and Yue (1987), is applied to model the first stages of growth of wave modulations (i.e., the longer lasting ones, on the order of 100 wave periods or more). The HOS solution is then used as initial condition for the 3D-NWT. Fourier methods were used to model extreme waves, e.g., by Baldock and Swan (1994) in 2D, and by Johannessen and Swan (1988) in 3D but, to our knowledge, a HOS method has not yet been applied to modeling 3D wave instabilities.

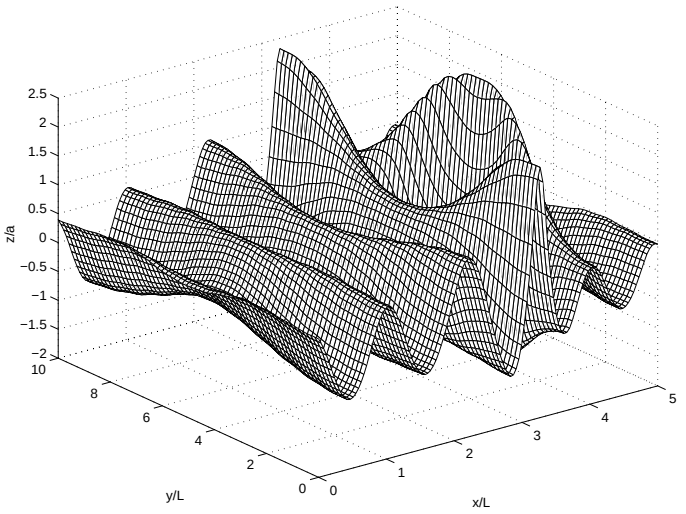

Fig. 2 : Modeling of the time evolution of a periodic wave train, modulated in both the longitudinal and transversal directions after 91 periods, using the HOS method.

The HOS method assumes doubly-periodic boundary conditions in the horizontal directions, in which a transversal (y) modulation is superimposed to a longitudinal (x) one. Similar periodicity conditions are specified in the 3D-NWT. Modulations of this type are characterized by the initial steepness of the wave train (ak), and two characteristic wavelenghts, for the longitudinal and transversal modulations, respectively. When the transversal modulation wavelength is sufficiently large, and after a sufficient propagation time, one can observe the growth of the lateral modulation through the absorption of part of the longitudinal wave energy. Fig. 2, for instance shows typical 3D wave modulations of a periodic wave train obtained after 91 periods, using the HOS method. We clearly see the appearance of a steep 3D wave. Note, the steeper the initial wavetrain, the more pronounced this effect. Thus, the modulational wavelengths are the fundamental parameters governing wave train evolution. Details of the application of the HOS method to 3D wave modulations can be found in Brandini (2001).

The modulation growth should be limited by wave breaking, which cannot be described by the HOS model. By introducing a solution such as obtained in Fig. 2 in the 3D-NWT, a very steep or even 3D breaking wave can be obtained after a small additional time of propagation in the NWT.

- Second, we model wave trains subjected to 3D directional wave focusing, including the additional possibility of frequency focusing such as studied earlier in 2D nonlinear models. To do so, a snake wavemaker similar to those used in laboratory facilities is modeled at one extremity of the 3D-NWT. A linear superposition of many directional wave trains, such as proposed by Dalrymple (1989), is specified at the wavemaker, with their phases (and/or frequency) calculated such that interference occurs at some specified distance away from the wavemaker.

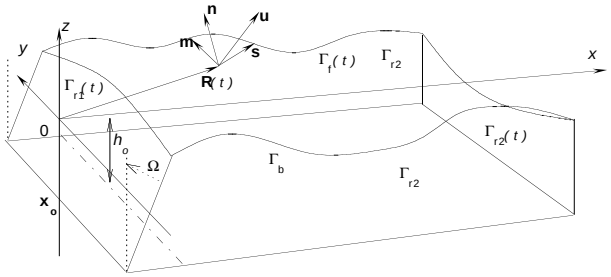

Fig. 3 : Sketch of NWT used for freak wave modeling by directional focusing using a snake wavemaker on boundary Γ_{r1} and a snake absorbing piston on boundary Γ_{r2}. The domain is of constant depth $h = h_o$. An image domain with respect to plane $z = -h_o$ is assumed. Tangential vectors at point $\mathbf{R}(t)$ of the free surface $\Gamma_f(t)$ are defined as $(\mathbf{s}, \mathbf{m})$ and outward normal vector as $\mathbf{n}$.

In the 3D-NWT's results, internal wave kinematics can be calculated for arbitrary locations and times, based on the boundary solution, including at or below the wave crest and within breaker jets. Using the NWT, we thus perform many 3D wave modulation and focusing numerical experiments, by varying problem parameters, and we study effects on extreme waves that are generated and on their kinematics.

THE NUMERICAL WAVE TANK

Governing equations and boundary conditions

Equations for fully nonlinear potential flows with a free surface are summarized below. The velocity potential is defined as $\phi(\mathbf{x}, t)$ and describes inviscid irrotational 3D flows in Cartesian coordinates $\mathbf{x} = (x, y, z)$, with z the vertical upward direction (and $z = 0$ at the undisturbed free surface; Fig. 1), and the velocity is defined by, $\mathbf{u} = \nabla\phi = (u, v, w)$.

Continuity equation in the fluid domain $\Omega(t)$, with boundary $\Gamma(t)$, is a Laplace's equation for the potential,

$$\nabla^2\phi = 0 \qquad \text{in } \Omega(t) \tag{1}$$

For constant depth, assuming an image domain with respect to plane $z = -h_o$, the 3D free space Green's function for Eq. (1) is defined as,

$$G = \frac{1}{4\pi}\left\{\frac{1}{r} + \frac{1}{r'}\right\} \;\; ; \;\; \frac{\partial G}{\partial n} = -\frac{1}{4\pi}\left\{\frac{\mathbf{r}\cdot\mathbf{n}}{r^3} + \frac{\mathbf{r}'\cdot\mathbf{n}'}{r'^3}\right\} \tag{2}$$

with $\mathbf{r} = \mathbf{x} - \mathbf{x}_l$, $\mathbf{r}' = \mathbf{r} - 2(h_o + z)\mathbf{k}$, and $r = \mid \mathbf{r} \mid$, $r' = \mid \mathbf{r}' \mid$, where $\mathbf{x}$ and $\mathbf{x}_l = (x_l, y_l, z_l)$ are points on boundary Γ, and $\mathbf{k}$ is the vertical unit vector, $\mathbf{n}$ is the outward unit vector normal to the boundary at point $\mathbf{x}$, and $\mathbf{n}'$ is defined from the components of vector $\mathbf{n}$, as $(n_x, n_y, -n_z)$.

Green's second identity transforms Eq. (1) into the Boundary Integral Equation (BIE),

$$\alpha_l\,\phi_l = \int_{\Gamma'} \left\{ \frac{\partial \phi}{\partial n}(\mathbf{x})\, G(\mathbf{x},\mathbf{x}_l) - \phi(\mathbf{x})\, \frac{\partial G}{\partial n}(\mathbf{x},\mathbf{x}_l) \right\} \mathrm{d}\Gamma' \quad (3)$$

in which $\alpha_l = \alpha(\mathbf{x}_l) = \theta_l/(4\pi)$, with θ_l the exterior solid angle made by the boundary at point $\mathbf{x}_l$ (i.e., 2π for a smooth boundary), and $\Gamma'(\mathbf{x})$ denotes boundary Γ minus the bottom boundary Γ_b.

The boundary is divided into various sections, with different boundary conditions (Fig. 3). On the free surface $\Gamma_f(t)$, ϕ satisfies the nonlinear kinematic and dynamic boundary conditions,

$$\frac{D\,\mathbf{R}}{D\,t} = \mathbf{u} = \nabla\phi \qquad \text{on } \Gamma_f(t) \quad (4)$$

$$\frac{D\,\phi}{D\,t} = -gz + \frac{1}{2}\,\nabla\phi\cdot\nabla\phi - \frac{p_a}{\rho_w} \qquad \text{on } \Gamma_f(t) \quad (5)$$

respectively, with $\mathbf{R}$ the position vector of a free surface fluid particle, g the acceleration due to gravity, p_a the atmospheric pressure, ρ_w the fluid density, and D/Dt the material derivative.

Various methods can be used in the NWT for wave generation. In the directional/frequency focusing experiments, waves are generated by simulating a "snake" flap wavemaker on the "open sea" boundary of the computational domain, $\Gamma_{r1}(t)$. Paddle position and velocity $[\mathbf{x}_p(t), \mathbf{u}_p(t)]$ are specified over the wavemaker as,

$$\overline{\mathbf{x}} = \mathbf{x}_p \;\;;\;\; \overline{\frac{\partial\phi}{\partial n}} = \mathbf{u}_p\cdot\mathbf{n} = \frac{\mathrm{d}\mathbf{x}_p}{\mathrm{d}\,t}\cdot\mathbf{n} \qquad \text{on } \Gamma_{r1}(t) \quad (6)$$

where overlines denote specified values, and the time derivative follows the wavemaker motion. See below for details. For periodic 3D wave instabilities, the initial wave elevation and velocity potential are specified at time t on the free surface, based on the HOS solution $[\eta_{HOS}(x,y,t), \phi_{HOS}(x,y,t)]$

$$\overline{z} = \eta_{HOS} \;\;;\;\; \overline{\phi} = \phi_{HOS} \qquad \text{on } \Gamma_f(t) \quad (7)$$

and space periodicity conditions are specified on lateral boundaries,

$$\begin{aligned} \overline{\frac{\partial\phi}{\partial n}}(x_{r2}) &= \frac{\partial\phi}{\partial n}(x_{r1}+L_x) \;\;;\;\; \overline{\phi}(x_{r2}) = \phi(x_{r1}+L_x) \\ \overline{\frac{\partial\phi}{\partial n}}(y_{r2}) &= \frac{\partial\phi}{\partial n}(y_{r1}+L_y) \;\;;\;\; \overline{\phi}(y_{r2}) = \phi(y_{r1}+L_y) \\ & \qquad\qquad \text{on } \Gamma_r(t) \end{aligned} \quad (8)$$

where $\Gamma_{r1}(t)$ and $\Gamma_{r2}(t)$ are vertical lateral boundaries perpendicular to the x and y axes, respectively, and L_x and L_y are perturbation wavelengths in the x and y directions, respectively.

Along stationary parts of the boundary, such as lateral parts of Γ_{r2} in the focusing experiment, a no-flow condition is prescribed as,

$$\overline{\frac{\partial\phi}{\partial n}} = 0 \qquad \text{on } \Gamma_{r2} \quad (9)$$

Note, using the image method, a no-flow condition is implicitly specified on the horizontal bottom boundary Γ_b.

For the wave focusing experiments, an actively absorbing boundary condition is specified at one extremity of the NWT, as a pressure sensitive "snake" absorbing piston (Clément, 1996; Grilli and Horillo, 1997). The piston normal velocity is specified as,

$$\overline{\frac{\partial\phi}{\partial n}} = u_{ap}(\sigma,t) \qquad \text{on } \Gamma_{r2}(t), \text{ with,} \quad (10)$$

$$u_{ap}(\sigma,t) = \frac{1}{\rho_w h_o \sqrt{g h_o}} \int_{-h_o}^{\eta_{ap}(\sigma,t)} p_D(\sigma,z,t)\,dz \quad (11)$$

calculated at the curvilinear abscissa σ, horizontally measured along the piston, where η_{ap} is the surface elevation at the piston and $p_D = -\rho_w\{\frac{\partial\phi}{\partial t} + \frac{1}{2}\nabla\phi\cdot\nabla\phi\}$ denotes the dynamic pressure. The integral in Eq. (11) represents the horizontal hydrodynamic force $F_D(\sigma,t)$ acting on the piston at time t, as a function of σ.

For well-posed problems, we have, $\Gamma' \equiv \Gamma_f \cup \Gamma_{r1} \cup \Gamma_{r2}$.

Time integration

Free surface boundary conditions (4) and (5) are integrated at time t to establish both the new position and the boundary conditions on the free surface $\Gamma_f(t)$ at a subsequent time $(t+\Delta t)$ (with Δt a varying time step).

To do so, second-order explicit Taylor series expansions are used to express both the new position $\mathbf{R}(t+\Delta t)$ and the potential $\phi(\mathbf{R}(t+\Delta t))$ on the free surface, in a MEL formulation (see Grilli *et al.*, 2001, for details). First-order coefficients in the Taylor series are given by Eqs. (4) and (5), which requires calculating $(\phi,\ \frac{\partial\phi}{\partial n})$ on the free surface. This is done by solving Eq. (3) at time t, with boundary conditions (6) to (11). Second-order coefficients are obtained from the material derivative of Eqs. (4) and (5), which requires also calculating $(\frac{\partial\phi}{\partial t},\ \frac{\partial^2\phi}{\partial t\partial n})$ at time t. This is done by solving a BIE similar to Eq. (3) for these fields. The free surface boundary condition for this second BIE is obtained from Bernoulli Eq. (4), after solution of the first BIE for ϕ as,

$$\overline{\frac{\partial\phi}{\partial t}} = -gz - \frac{1}{2}\nabla\phi\cdot\nabla\phi - \frac{p_a}{\rho_w} \qquad \text{on } \Gamma_f(t) \quad (12)$$

For a wave generation by a wavemaker, Eq. (6) gives,

$$\overline{\frac{\partial^2\phi}{\partial t\partial n}} = \frac{\partial(\mathbf{u}_p\cdot\mathbf{n})}{\partial t} \qquad \text{on } \Gamma_{r1}(t) \quad (13)$$

and for stationary boundaries,

$$\overline{\frac{\partial^2\phi}{\partial t\partial n}} = 0 \qquad \text{on } \Gamma_{r2} \quad (14)$$

For the self-focusing problem, periodicity conditions such as Eq. (8) are expressed for $\frac{\partial^2\phi}{\partial t\partial n}$, and for the directional/frequency focusing, an absorbing condition is expressed from Eq. (11) as,

$$\overline{\frac{\partial^2\phi}{\partial t\partial n}} = \frac{\partial u_{ap}(\sigma,t)}{\partial t} \qquad \text{on } \Gamma_{r2}(t) \quad (15)$$

Time step Δt in the Taylor series is adapted at each time as a function of the minimum distance between nodes on the free surface and of a constant mesh Courant number $\mathcal{C}_o \simeq 0.5$ (see Grilli *et al.*, 2001, for details).

Discretization, numerical integrations, solution

The discretization follows that of Grilli *et al.*'s (2001) model, where all details can be found.

The BIEs for ϕ and $\frac{\partial \phi}{\partial t}$ are solved by a Boundary Element Method (BEM). The boundary is discretized into collocation nodes and higher-order elements are used to interpolate in between these nodes. The boundary geometry and the field variables are discretized over the elements using polynomial shape functions. These functions are analytically defined over a single reference element. To provide sufficient continuity, boundary elements are defined with cubic shape functions expressed over 4 by 4 node patches, of which only one 4-node quadrilateral is used as the boundary element. Hence, only a part of the interval of variation (usually the middle part, unless nodes are close to a boundary intersection) of the cubic shape functions is used for calculating the boundary integrals in Eq. (3).

Details of curvilinear changes of variables needed for expressing boundary integrals over reference elements, and final dicretized equations, are left out due to lack of space.

Discretized boundary integrals are calculated for each collocation node by numerical integration. When the collocation node does not belong to the integrated quadrilateral element, a standard Gauss-Legendre quadrature method is used. When this node belongs to the element, distance r in the Green's function, and its normal gradient, becomes zero at one of the nodes of the element (Eq. (2)). The weakly singular integrals including $1/r$ are transformed with a method of "singularity extraction" based on polar coordinate and other transformations, and then numerically integrated by Gauss quadrature; again, details are left out due to lack of space.

Boundary conditions and normal directions are in general different on intersecting parts of the boundary, such as between the free surface and the lateral boundary of the computational domain (Fig. 1). Such intersections are referred to as edges, and corresponding discretization nodes as corners. To be able to specify such differences, corners are represented in the model by double-nodes, for which coordinates are identical but normal vectors are different. Thus, two different discretized BIEs are expressed for each node of a corner double-node. Since the potential (and its time derivative) must be identical for each node of a double node, one of the two BIEs in the discretized system of equations is modified to express this condition. The same technique is used for triple-nodes, representing intersections between three boundaries.

The solution of the algebraic system, used in the applications presented hereafter, is based on a direct elimination method, for which the CPU time is proportional to the cube of the number of nodes in the discretization.

Tangential derivatives

Tangential derivatives, e.g., needed in the Taylor series, are calculated on the boundary in a local curvilinear coordinate system $(\mathbf{s}, \mathbf{m}, \mathbf{n})$ defined at each boundary node (Fig. 1), with $\mathbf{s} = \mathbf{x}_s$, $\mathbf{m} = \mathbf{x}_m$, and $\mathbf{n} = \mathbf{s} \times \mathbf{m}$ (subscripts indicate partial derivatives). Derivatives of the geometry and field variables in tangential directions $\mathbf{s}$ and $\mathbf{m}$ are computed, by defining, around each node, a local 5 by 5 node, 4th-order, sliding element and differentiating within it (see Grilli *et al.*, 2001, for details).

Because of the difference between partial, material, or time derivatives following a boundary motion, it is necessary to further develop equations such as (13) and (15). For a wavemaker, we find, from Eq. (13) with Eq. (6) for ϕ_n,

$$\overline{\frac{\partial^2 \phi}{\partial t \partial n}} = (\frac{\mathrm{d}\mathbf{u}_p}{\mathrm{d}t} \cdot \mathbf{n}) + (\mathbf{u}_p \cdot \frac{\mathrm{d}\mathbf{n}}{\mathrm{d}t}) - \phi_n \phi_{nn} - (\mathbf{u}_p \cdot \mathbf{s})\, \phi_{ns} - (\mathbf{u}_p \cdot \mathbf{m})\, \phi_{nm} \tag{16}$$

with,

$$\phi_{nn} = -\phi_{ss} - \phi_{mm} + \phi_s \{\mathbf{x}_{ss} \cdot \mathbf{s} - \mathbf{x}_{sm} \cdot \mathbf{m}\} + \phi_m \{\mathbf{x}_{mm} \cdot \mathbf{m} - \mathbf{x}_{sm} \cdot \mathbf{s}\} + \phi_n \{\mathbf{x}_{ss} \cdot \mathbf{n} + \mathbf{x}_{mm} \cdot \mathbf{n}\} \tag{17}$$

where, $\mathrm{d}\mathbf{u}_p/\mathrm{d}t$ denotes the absolute wavemaker acceleration, and $\mathrm{d}\mathbf{n}/\mathrm{d}t = \dot{\Omega}\, \mathbf{j} \times \mathbf{n}$, for instance, for a wavemaker rotating with angular velocity $\dot{\Omega}(y,t)$ around axis y of unit direction $\mathbf{j}$. [Note, upper dots indicate time derivatives $\mathrm{d}/\mathrm{d}t$ following the wavemaker motion.]

From Eq. (15), we find for the snake absorbing piston, assuming its motion follows that of water particles,

$$\overline{\frac{\partial^2 \phi}{\partial t \partial n}} = \frac{D\, u_{ap}}{D\, t} - \phi_s \phi_{ns} - \phi_m \phi_{nm} - \phi_n \phi_{nn} \tag{18}$$

with ϕ_{nn} given by Eq. (17). The material derivative of the piston velocity is simply calculated by backward finite differentiation of Eq. (11). The piston position is calculated for the next time step using a Taylor series expansion similar to the free surface's,

$$x_{ap}(\sigma, t + \Delta t) = x_{ap} + u_{ap}\, n_x\, \Delta t + \frac{D\,(u_{ap}\, n_x)}{D\, t} \frac{(\Delta t)^2}{2} \tag{19}$$

where the right-hand-side is evaluated at (σ, t), and n_x denotes the normal vector's x-component.

APPLICATIONS

Due to lack of space, applications presented here will be limited to freak waves produced by 3D directional wave energy focusing. These are cases involving both the newly developed snake flap wavemaker and snake absorbing piston boundaries. Applications for periodic cases of self-focusing instabilities which, in fact, have simpler features from the point of view of the NWT will be left out for future papers.

Wavemaker motion for 3D wave focusing

For a flap snake wavemaker located on boundary Γ_{r1}, we define the wavemaker paddle position $\mathbf{x}_p = (x_p, y_p, z_p)$ as (Fig. 3),

$$\mathbf{x}_p = \mathbf{x}_o - \rho\,\mathbf{m} \quad , \text{with} \quad \mathbf{x}_o = y_p\,\mathbf{j} - h_o\,\mathbf{k} \tag{20}$$

the coordinates of the paddle axis of rotation, where the angular velocity $\dot{\Omega}\,\mathbf{j}$ is applied. Symbol ρ denotes the distance from the axis of rotation, measured on the wavemaker in vertical planes. Hence,

$$\rho = \sqrt{x_p^2 + (h_o + z_p)^2} \quad , \text{and} \quad \Omega = \arctan\frac{S_o}{h_o} \tag{21}$$

where $S_o(y,t)$ denotes the horizontal wavemaker stroke specified at $z = 0$. From these definitions, we find,

$$\begin{aligned} \mathbf{u}_p &= -\dot{\rho}\,\mathbf{m} - \rho\,\dot{\Omega}\,\mathbf{n} \\ \frac{\mathrm{d}\mathbf{u}_p}{\mathrm{d}t} &= (\rho\,\dot{\Omega}^2 - \ddot{\rho})\,\mathbf{m} - (2\,\dot{\rho}\,\dot{\Omega} + \rho\,\ddot{\Omega})\,\mathbf{n} \end{aligned} \tag{22}$$

Introducing Eq. (22) into Eqs. (6) and (16), we find, for the wavemaker boundary conditions as,

$$\overline{\frac{\partial\phi}{\partial n}} = -\rho\,\dot{\Omega} \quad , \text{and} \quad \overline{\frac{\partial^2\phi}{\partial t\,\partial n}} = -\rho\,\ddot{\Omega} + \rho\,\dot{\Omega}\,\phi_{nn} \tag{23}$$

where ϕ_{nn} is given by Eq. (17), with $\mathbf{x}_{sm} = \mathbf{x}_{mm} = 0$.

Following Dalrymple (1989), we specify the wavemaker stroke as the linear superposition of N_θ sinusoidal components of amplitude a_n and direction θ_n, as,

$$S_o = \sum_{n=1}^{N_\theta} a_n\,\cos\left\{k_n\,(y\sin\theta_n - x_f\cos\theta_n) - \omega_n t\right\} \tag{24}$$

where k_n and ω_n denote components' wavenumber and wave frequency, related by the linear dispersion relationship,

$$\omega_n^2 = g\,k_n\,\tanh\left(k_n h_o\right) \tag{25}$$

and x_f is the focusing distance for the waves in front of the wavemaker. Angles θ_n are uniformly distributed in the range $[-\theta_{\max}, \theta_{\max}]$.

In the applications below, only directional wave focusing is presented, hence $\omega_n = \omega$ and, for simplicity, we specify stroke components with identical amplitudes $a_n = A$. Additional frequency focusing could be achieved by adjusting the wave frequency as a function of the angle, for instance, as $\omega_n = k_n\,c_o/\cos\theta_n$ (with c_o the celerity of the wave of frequency ω_o and angle $\theta_o = 0$).

Directional 3D wave focusing : non-breaking case

In the following, non-dimensional variables are used, and denoted by dashes, in which lengths are divided by h_o and times by $\sqrt{h_o/g}$. Directional wave energy focusing is simulated in a NWT of depth $h'_o = 1$ (with $g' = \rho'_w = 1$), initial length $l'_o = 10$ and width $w'_o = 16$. Due to symmetry in the y direction, only half the NWT width is discretized with boundary elements. We use 20 elements in the x direction, of length $\Delta x'_o = 0.5$, 16 elements in the half-width y direction, of length $\Delta y'_o = 0.5$, and 4 elements over the depth, with height $\Delta z'_o = 0.25$. For a Courant number of 0.45, the initial time step is set to $\Delta t'_o = 0.225$. The total number of nodes is 737 and there are 608 elements. With this data, the CPU time per time step is 2'20" on a Mac G4-450MHz.

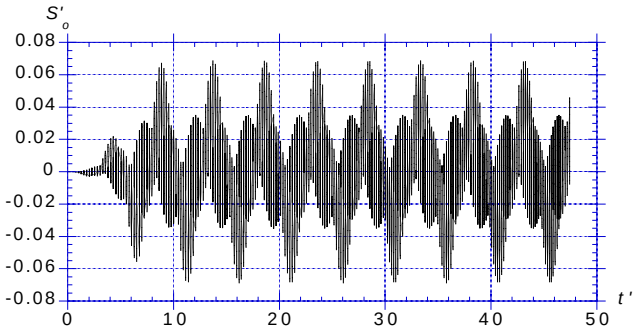

Fig. 4 : Snake wavemaker stroke as a function of time for $N_\theta = 4$, $\theta_{\max} = 25°$, $\omega'_n = \omega' = 1.2816$, $a'_n = A' = 0.02$, and $x'_f = 7.45$.

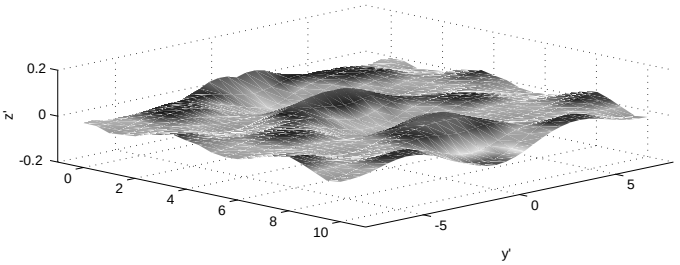

Fig. 5 : Free surface calculated at $t' = 36.66$ for the incident wave of Fig. 4. Darker areas have the highest and lowest elevations.

We specify a snake wavemaker, initially located at $x' = 0$, and prescribe its motion according to Eqs. (20) to (25), using $N_\theta = 4$ wave components, with $\theta_{\max} = 25°$, $\omega'_n = \omega' = 1.2816$, and $a'_n = A' = 0.02$. With this data, we find the linear wavenumber $k'_n = k = 1.6866$, to which it corresponds a linear wavelength $L' = 3.725$. Wave focusing is specified at a distance $x'_f = 2L' = 7.45$ in front of the wavemaker. To reduce initial singularity problems, as done in similar 2D models (e.g., Grilli and Horrillo, 1997), the stroke S'_o is multiplied by a tanh function, which ramps-up the wavemaker motion from zero to its maximum value over a given time; here, this time is specified to $2T'$, where $T' = 4.903$ is the wave period.

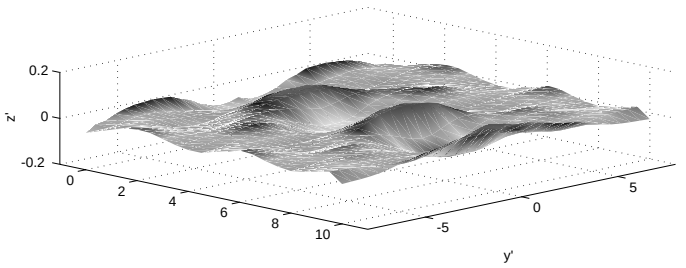

Fig. 6 : Same case as Fig. 5 for $t' = 39.90$.

We also specify an absorbing snake piston boundary condition at the extremity of the NWT, initially at $x' = l'_o$, according to Eqs. (10), (11), (18) and (19). Fig. 4 shows the calculated wavemaker stroke for the 17 discretization nodes in the y direction, Fig. 5 shows the free surface obtained after 165 time steps, at $t' = 36.66$, over the full width of the NWT, and Fig. 6 shows the same results after 181 steps, at $t' = 39.90$. It is clear in Figs. 5 and 6 that large waves periodically occur in the middle of the NWT at $y' = 0$, due to directional energy focusing. Fig. 7 shows results obtained for numerical wave gages located on the x axis. One first sees that a fairly periodic signal is obtained at the gages, which indicates that there is little reflection coming back from the absorbing boundary (at least during the computed time interval). Second, it is clear that a larger wave is obtained at $x' = 7.45$ than at other gages in the tank. This is expected from the parameters specified at the wavemaker. Finally, Fig. 8 shows results at wave gages located off the y axis, and we see that much smaller waves are obtained there, further confirming the energy focusing towards the middle of the NWT.

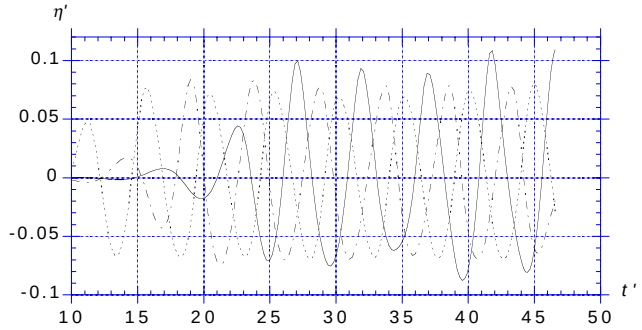

Fig. 7 : Same cases as Fig. 4-6. Numerical wave gages at $y' = 0$ and $x' = 2.5$ (- - - - -); 5.0 (— - —); 7.45 (———).

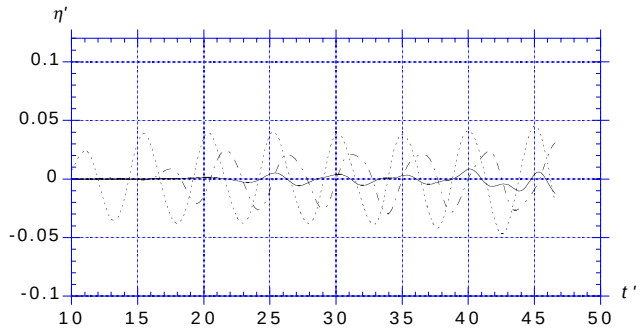

Fig. 8 : Same cases as Fig. 4-7. Numerical wave gages at (x', y') : (2.5,-2.0) (- - - - -); (5.0,-4.0) (— - —); (7.45,-6.0) (———).

During these computations, the error on continuity equation was calculated at each time step by integrating the boundary fluxes. This error was transformed into a volume error by multiplying by the time step, i.e., $\Delta V = \Delta t \int \phi_n d\Gamma$, and made dimensionless by dividing it by the wave volume defined as, $V_w = \int \mid \eta \mid d\Gamma_f$, i.e., $\varepsilon_c(t) = \mid \Delta V \mid / V_w$. The instantaneous maximum of this error was less than 0.012%. Only 7-8 nodes/elements, however, were used per wavelength in these computations, and it is expected that errors would further decrease by reducing the size of the elements (see Grilli *et al.*, 2001 for details of convergence properties of the NWT). The maximum relative volume change of the computational domain at the end of the computations was 0.19%, which both includes an error and the displacement of the absorbing piston.

Directional 3D wave focusing : breaking case

We now simulate a case with more intense directional energy focusing, producing one giant breaking wave. The initial domain length is $l'_o = 4$, the width is $w'_o = 8$, and the depth is $h'_o = 1$. Due to breaking, the symmetry in the y direction can no longer be used to reduce the problem size, as element wrap-up would occur on one sidewall of the NWT. We use 20 elements in the x direction, of length $\Delta x'_o = 0.2$, 40 elements in the width y direction, of length $\Delta y'_o = 0.2$, and 6 elements over the depth, with height $\Delta z'_o = 0.167$. For a Courant number of 0.45, the initial time step is set to $\Delta t'_o = 0.09$. The total number of nodes is 1,729 and there are 1,520 elements. With this data, the CPU time per time step is 15'33" on a Mac G4-450MHz.

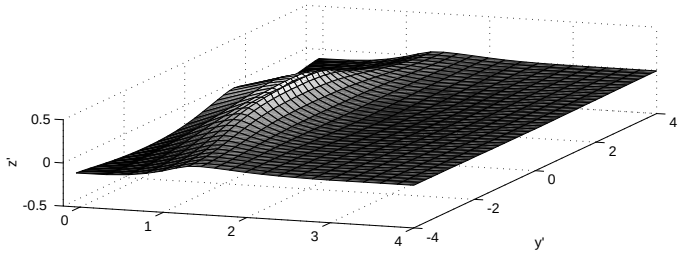

Fig. 9 : Free surface calculated at $t' = 8.89$ for $N_\theta = 8$, $\theta_{\max} = 30°$, $\omega'_n = \omega' = 1.2816$, $a'_n = A' = 0.05$, and $x'_f = 7.45$.

The snake wavemaker parameters are : $N_\theta = 8$ wave components, with $\theta_{\max} = 30°$, $\omega'_n = \omega' = 1.2816$, and $a'_n = A' = 0.05$. Other data and boundary conditions are as in the previous case. Fig. 9 shows the free surface obtained after 130 time steps in the NWT, at $t' = 8.89$, i.e., after almost two periods of motion of the wavemaker. We see that one large steep wave is produced a short distance

away from the wavemaker, whose crest is starting to break by spilling breaking. Intense node converging occurs in the breaker crest, however, which causes quasi-singularities in the BEM equations, due to node proximity. Hence, computations had to be interrupted shortly after the time of Fig. 9, before crest overturning occurred. This could be eliminated by selective node regridding of the free surface (see Grilli *et al.*, 2001 for details). For these computations, the maximum instantaneous error on continuity was $\varepsilon_c^{\max} = 0.0014\%$, and the maximum relative volume change was 0.047%.

CONCLUSIONS

Extreme (freak) wave generation mechanisms were explored using a Numerical Wave Tank (NWT) solving fully nonlinear potential flow theory. Two main types of three-dimensional wave energy focusing, leading to freak wave generation, were presented and discussed : (i) self-focusing instabilities; (ii) directional/frequency focusing for curved wave trains. Applications were only presented for the latter case, due to lack of space. New features were added to the NWT (snake wavemaker, snake absorbing piston, periodicity conditions). In directional focusing, waves are focused in front of the wavemaker. We present both non-breaking and breaking cases. Characteristics of such huge waves, such as flow kinematics, important for the design of offshore structures, can be explored in these simulations, as well as conditions leading to the occurrence of worst case scenarios. In particular, the self-focusing case can be studied in the NWT, which would be very difficult to do in the laboratory, due to the long distances of propagation required for the instabilities to grow.

REFERENCES

Baldock, T.E., Swan, C. (1994). "Numerical calculations of large transient water waves," *Appl. Ocean Res.*, Vol 16, pp 101-112.

Brandini, C. (2001). *Nonlinear Interaction Processes in Extreme Wave Dynamics*. Ph.D. Dissertation. University of Firenze.

Brandini, C. and S.T. Grilli (2000). "On the numerical modeling of extreme highly nonlinear deep water waves," *Proc. IABEM 2000 Symp.* (Brescia, Italy, July 2000), pp 54-58.

Benjamin, T.B. and J.E., Feir (1967). "The disintegration of wave trains on deep water. Part 1. Theory," *J. Fluid Mech.*, Vol 27, pp 417-430.

Chaplin, J.R. (1996). "On frequency-focusing unidirectional waves," *Intl. J. Offshore and Polar Engng.*, Vol 6, pp 131-137.

Clément, A. (1996). "Coupling of two absorbing boundary conditions for 2D time-domain simulations of free surface gravity waves," *J. Comp. Phys.*, Vol 26, pp 139-151.

Dalrymple, R.A. (1989). "Directional wavemaker theory with sidewall reflection," *J. Hydraulic Res.*, Vol 27(1), pp 23-34.

Dean, R.G. (1990). "Freak waves: a possible explanation," *Water Wave Kinematics* (ed. A.Torum and O.T. Gudmestad), Kluwer, pp 609-612.

Dold J.W. and D.H., Peregrine (1986). "Water-wave modulation," *Proc. 20th Intl. Conf. Coast. Engng.*, ASCE, pp 163-175.

Dommermuth, D.G. and D.K.P., Yue (1987). "A higher-order spectral method for the study of non linear gravity waves," *J. Fluid Mech.*, Vol 184, pp 267-288.

Dommermuth, D.G., Yue, D.K.P., Lin, W.M., Rapp, R.J., Chan, E.S. and W.K., Melville (1988). "Deep-water plunging breakers : a comparison between potential theory and experiments," *J. Fluid Mech.*, Vol 189, pp 423-442.

Dysthe, K.B. and K., Trulsen (1999). "Note on breather type solutions of the NLS as model for freak waves," *Phys. Scripta*, Vol T82, pp 45-73.

Grilli, S.T., Guyenne, P. and F., Dias (2000). "Modeling of overturning waves over arbitrary bottom in a 3D numerical wave tank," *Proc. 10th Offshore and Polar Engng. Conf.* (ISOPE00, Seattle, USA, May 2000), ISOPE, Vol III, pp 221-228.

Grilli, S.T., Guyenne, P. and F., Dias (2001). "A fully nonlinear model for three-dimensional overturning waves over arbitrary bottom," *Intl. J. Numer. Methods in Fluids*, Vol 34, 39 pps (in press).

Grilli, S.T. and J., Horrillo (1997). "Numerical generation and absorption of fully nonlinear periodic waves." *J. Engng. Mech.*, Vol 123(10), pp 1060-1069.

Johannessen, T.B., and C., Swan (1998). "Extreme multidirectional waves," *Proc. 26th Intl. Conf. Coast. Engng.*, ASCE, pp 1110-1123.

Kjeldsen, S.P., Drenman, W.M., and M.G., Skafel (2000). "Modeling of velocities in giant waves," *Intl. J. Offshore and Polar Engng.*, Vol 10(3), pp 170-172.

McLean, J.W. (1982). "Instabilities and breaking of finite amplitude waves," *J. Fluid Mech.*, Vol 114, pp 315-341.

Nepf, H.M., Wu, C.H., and E.S., Chan (1998). "A comparison of two- and three-dimensional wave breaking," *J. of Phys. Oceanography*, Vol 28, pp 1496-1510.

Henderson, K.L., Peregrine, D.H., and J.W., Dold (1999). "Unsteady water wave modulations : fully non linear solutions and comparison with the non linear Schrödinger equation," *Wave motion*, Vol 9, pp 341-361.

Sand, S.E., Ottesen Hansen, N.E., Klinting, P., Gudmestad, O.T. and M.J., Sterndorff (1990). "Freak waves kinematics. *Water Wave Kinematics* (ed. A.Torum and O.T. Gudmestad), Kluwer , pp 535-548.

She, K., Greated, C.A. and W.J., Easson (1997). "Experimental study of three-dimensional breaking wave kinematics," *Appl. Ocean Res.*, Vol 19, pp 329-343.

Skourup, J., Hansen, N-E.O. and K.K., Andreasen (1997). "Non-Gaussian extreme waves in the central North Sea," *Trans. ASME*, Vol 119, pp 146-150.

Su, M.Y., Bergin, M., Marler, P. and R., Myrick (1982) Experiments on nonlinear instabilities and evolution of steep gravity-wave trains," *J. Fluid Mech.*, Vol 124, pp 45-72.

White, B.S. and B., Fornberg (1998). "On the chance of freak waves at sea," *J. Fluid Mech.*, Vol 355, pp 113-138.